Research Article

Sungho Yun, Dowon Cha, Kang Sub Song, Seong Ho Hong, Sang Hun Lee, Wonseok Yang, and Yongchan Kim*

Numerical analysis on the dynamic response of a plate-and-frame membrane humidifier for PEMFC vehicles under various operating conditions

https://doi.org/10.1515/phys-2018-0081
Received Sep 18, 2017; accepted Jul 04, 2018

Abstract: A PEMFC needs to be maintained at an appropriate temperature and humidity in a rapidly changing environment for automobile applications. In this study, a pseudo-multi-dimensional dynamic model for predicting the heat and mass transfer performance of a plate-and-frame membrane humidifier for PEMFC vehicles is developed. Based on the developed model, the variations in the temperature and relative humidity at the dry air outlet are investigated according to the air flow acceleration. Moreover, the dynamic response is analyzed as a function of the amplitude and period of the sinusoidal air flow rate at actual operating conditions. The effects of heat transfer on the dynamic response are more dominant than those of mass transfer. The settling time of the temperature and relative humidity at the dry air outlet decrease with the increase in air flow acceleration. In addition, the variations in the temperature and relative humidity at the dry air outlet increase with the increases in the amplitude and period of the sinusoidal air flow rate.

Keywords: Dynamic response, Heat and mass transfer, Numerical model, PEMFC, Plate-and-frame membrane humidifier

PACS: 44.05.+e, 44.27.+g, 88.30.gg, 88.30.pd

Nomenclature

A_{amp} amplitude (g s^{-1})
A_{fr} fractional area (m^2)
a_v water activity (-)
B_{peri} period (s)
C heat capacity ratio (J $s^{-1}K^{-1}$)
c_p heat capacity (J $kg^{-1}K^{-1}$)
D_g water diffusivity in the gas phase (m^2 s^{-1})
D_h hydraulic diameter (m)
D_w water diffusivity (kg $m^{-1}s^{-1}$)
h convective heat transfer coefficient (W $m^{-2}K^{-1}$)
h_m convective mass transfer coefficient (kg $m^{-2}s^{-1}$)
k thermal conductivity (W $m^{-1}K^{-1}$)
Le Lewis number (-)
$\dot{m}$ mass flow rate (kg s^{-1})
Nu Nusselt number (-)
P pressure (bar)
U overall heat transfer coefficient (W $m^{-2}K^{-1}$)
V velocity (m s^{-1})
S perimeter (m)
Sh Sherwood number (-)

Greek symbols

Δ difference (-)
δ thickness (m)
λ water content (-)
ρ density (kg m^{-3})
φ relative humidity (%)

Subscripts

d dry air
global global value
in inlet

***Corresponding Author: Yongchan Kim:** Department of Mechanical Engineering, Korea University, Anam-Dong, Sungbuk-Ku, Seoul, 02841, Republic of Korea; Email: yongckim@korea.ac.kr; Tel.: +82-2-3290-3366; Fax: +82-2-921-5439

Sungho Yun, Dowon Cha, Kang Sub Song, Seong Ho Hong, Sang Hun Lee, Wonseok Yang: Department of Mechanical Engineering, Korea University, Anam-Dong, Sungbuk-Ku, Seoul, 02841, Republic of Korea

m membrane
max maximum value
min minimum value
out outlet
p plate
sat saturation
v vapor
w wet air

Acronyms

MFF mass flow rate factor
PEMFC proton exchange membrane fuel cells

1 Introduction

Proton exchange membrane fuel cells (PEMFCs) can be utilized in the power supply for portable systems, stationary systems, vehicles, spacecraft, and other special applications owing to their high power density, high efficiency, and modular nature [1, 2]. In particular, owing to their lower operating temperature, higher power density, and shorter start-up time, various studies on PEMFC vehicles are occurring in major automobile companies [3–5]. However, the PEMFC need to be maintained at an appropriate temperature and humidity in the rapidly changing environment associated with automobile applications [6].

Studies involving various types of humidifiers have been conducted in order to control the temperature and relative humidity of the supply air [7–10]. Extensive studies have been also conducted on bubbling, water spray, enthalpy wheel, and membrane humidifiers. From these types, membrane humidifiers are the most suitable for PEMFC vehicles due to their fast response and simplicity. Recently, case studies have been carried out to apply membrane humidifiers to PEMFC systems [11–14]. Membrane humidifiers are categorized as either shell-and-tube or plate-and-frame membrane humidifiers depending on the shape [15, 16]. Park [17] presented a dynamic model of a shell-and-tube membrane humidifier. Kang [18] investigated the performance of a shell-and-tube membrane humidifier for PEMFC vehicles. However, the shell-and-tube membrane humidifier has the disadvantages of a bulky volume and difficulty in mass production. Accordingly, studies on the plate-and-frame membrane humidifier are underway to overcome these drawbacks.

Zhang [19] proposed an effectiveness-correlation model for a plate-and-frame membrane humidifier, in order to analyze the heat and mass transfer processes in an enthalpy exchanger. Several studies verified the effectiveness-correlation model for the enthalpy exchanger [20–22]. Kadylak [23] discussed limitations on the application of the effectiveness-correlation model to the plate-and-frame membrane humidifier. Kadylak [24] also experimentally validated the developed effectiveness-correlation model with a plate-and-frame membrane. However, the effectiveness-correlation model showed some limitations for analyzing the dynamic response of a plate-and-frame membrane humidifier. Accordingly, there is a need to develop a novel model for predicting the dynamic response of a plate-and-frame membrane humidifier for PEMFC vehicles under actual operating conditions. In particular, the temperature variations due to air entering the plate-and-frame membrane humidifier according to the air flow rate need to be considered.

Numerical and experimental studies analyzing the phenomena in the plate-and-frame membrane humidifier have also been carried out. Yu [25] proposed a static model for a counter flow plate-and-frame membrane humidifier. Ahluwalia [26] conducted static and dynamic tests on a plate-and-frame membrane humidifier. Even though these studies developed a finite-difference model, the heat transfer, which is a main dynamic mechanism in the plate-and-frame humidifier, was not considered in the plate. Moreover, in the existing studies, a multi-dimensional dynamic model was not applied for a plate-and-frame membrane humidifier, which has multi-dimensional structures stacked with multiple membranes and plates for PEMFC vehicles [17, 27].

In this study, a pseudo-multi-dimensional dynamic model was developed for predicting the dynamic response of a plate-and-frame membrane humidifier with a plate domain. This model incorporated one-dimensional heat transfer in the plate, one-dimensional heat and mass transfer in the membrane, and one-dimensional thermo-fluid channel in the plate-and-frame membrane humidifier. Based on the proposed model, the dynamic response of the plate-and-frame membrane humidifier for PEMFC vehicles was analyzed under various operating conditions. The variations in the temperature and relative humidity at the dry air outlet were investigated in accordance with air flow acceleration. The temperature changes in the membrane and plate were also examined to evaluate the overshoot and settling time. Moreover, the dynamic response of the plate-and-frame membrane humidifier was analyzed as a function of the amplitude and period of the sinusoidal air flow rate under actual operating conditions.

2 Numerical model

As shown in Figure 1, the plate-and-frame membrane humidifier has multiple membranes and plates. It is a heat and mass exchanger with a water-permeable polymer membrane installed in between dry and wet air. Table 1 shows geometric configurations of the computational model and humidifier. The channel width, channel height, and channel length were determined from the tested plate-and-frame membrane humidifier in the previous study [25]. In addition, the number of channels in the plate and number of plates were designed to satisfy the rated capacity of 100 kW in a PEMFC system. Figure 2 shows the computational domain of the plate-and-frame membrane humidifier. In the numerical analysis, the wet air and dry air were discretized in their individual flow directions.

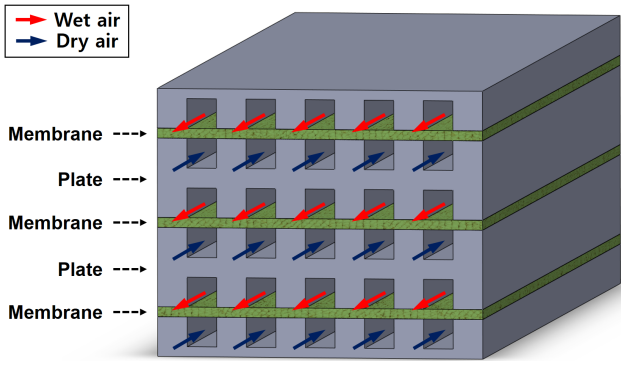

Figure 1: Schematic of the plate-and-frame membrane humidifier

Table 1: Geometric parameters of the plate-and-frame membrane humidifier

Parameters	Value
Channel width	0.003 m
Channel height	0.003 m
Channel length	0.322 m
Number of channels in the plate	34
Number of plates	90
Plate thickness	0.001 m
Membrane thickness (Nafion®)	5.1×10^{-5} m

The numerical model has been developed based on the following assumptions [15, 18]: (1) the flow in the air channel is incompressible and laminar; (2) phase change is ignored; (3) physical properties are constant along the length of the humidifier; (4) the velocity is constant in the axial direction and the velocity profile is fully developed; and (5) the vapor diffusion in the membrane occurs only in the normal direction. Algebraic heat and mass transfer equations were solved simultaneously by using the Gauss-Seidel method based on an upwind finite-difference scheme in Visual Fortran 6.0.

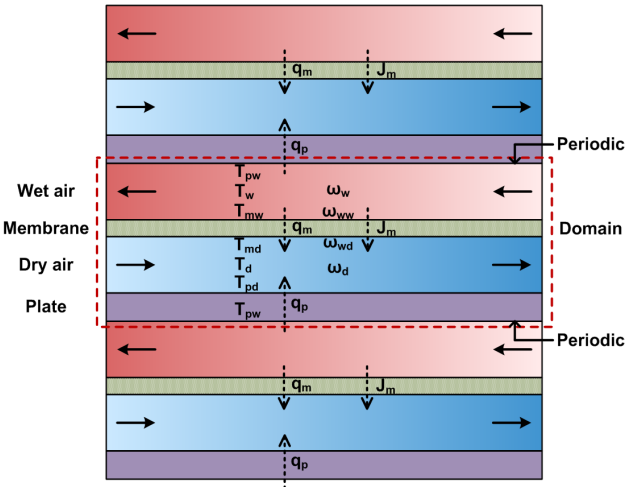

Figure 2: Computational domain of the plate-and-frame membrane humidifier

2.1 Heat transfer

The plate-and-frame membrane humidifier consists of the wet air, dry air, membrane, and plate domains. The wet air domain contains humid air flow discharged from the PEMFC, whereas the dry air domain includes a dry air flow path in which the ambient air flows into an air humidifier using an air blower. In these domains, the forced convective heat transfer is dominant. On the other hand, the conduction heat transfer is dominant in the plate and membrane domains.

The energy balance equations for the wet air, membrane, dry air, and plate domains in the plate-and-frame membrane humidifier are expressed by Eqs. (1)–(4) [28, 29], respectively:

$$C_w\frac{dT_w}{dx} - U_wS_w(T_w - T_m) - U_dS_d(T_p - T_d) = -\frac{C_w}{V_w}\frac{\partial T_w}{\partial t} \quad (1)$$

$$U_dS_d(T_m - T_d) - U_wS_w(T_w - T_m) = -c_{p,m}\rho_m\delta_mS_m\frac{\partial T_m}{\partial t} \quad (2)$$

$$C_d\frac{dT_d}{dx} + U_wS_w(T_w - T_m) + U_dS_d(T_m - T_d) \quad (3)$$

$$= -\frac{C_d}{V_d}\frac{\partial T_d}{\partial t}$$

$$U_d S_d(T_p - T_d) - U_w S_w(T_w - T_p) = -c_{p,p}\rho_p \delta_p S_p \frac{\partial T_p}{\partial t} \quad (4)$$

where U is the overall heat transfer coefficient, S is the perimeter, and δ is the thickness. The heat capacity ratio (C) is given as:

$$C_w = c_{p,w}\rho_w A_{fr,w} V_w \quad (5)$$

$$C_d = c_{p,d}\rho_d A_{fr,d} V_d \quad (6)$$

As given in Eq. (7), the convective heat transfer coefficient is constant in the fully developed laminar flow [28]:

$$Nu = 3.61 \quad (7)$$

$$Nu = \frac{hD_h}{k} \quad (8)$$

where D_h is the hydraulic diameter and k is the thermal conductivity.

2.2 Mass transfer

The mass balance equations for the wet air, membrane, and dry air domains are given by Eqs. (9)–(11), respectively:

$$V_w \frac{d\omega_w}{dx} - h_{M,w} S_w(\omega_w - \omega_{mw}) = -\frac{\partial \omega_w}{\partial t} \quad (9)$$

$$\frac{\partial}{\partial z}\left(D_w \frac{\partial \omega_m}{\partial z}\right) = \frac{d\omega_m}{dt} \quad (10)$$

$$V_d \frac{d\omega_d}{dx} + h_{M,d} S_d(\omega_{md} - \omega_d) = -\frac{\partial \omega_d}{\partial t} \quad (11)$$

where ω is the absolute humidity and h_M is the mass transfer coefficient. In addition, the diffusion coefficient (D_w) is given as [30]:

$$D_w = 3.1 \cdot 10^{-3}\lambda(-1 + e^{-2436/T}) : 0 < \lambda \le 3 \quad (12)$$

$$D_w = 4.17 \cdot 10^{-4}\lambda(1 + 161e^{-\lambda})e^{-2436/T} : 3 \le \lambda < 17 \quad (13)$$

As given in Eqs. (14) and (15), the water content (λ) is determined by the water activity (a_v) [30]:

$$\lambda = 0.3 + 10.8 \cdot a_v - 16 \cdot {a_v}^2 + 14.1 \cdot {a_v}^3 \quad (14)$$

$$a_v = \frac{x_v p}{p_{sat,v}} \quad (15)$$

As given in Eqs. (16) and (17), the mass transfer coefficient (h_M) can be obtained from the relationship between Sherwood number and Nusselt number [15]:

$$Sh = \frac{h_M D_h}{D_g} \quad (16)$$

$$Sh = Nu\,(Le)^{-1/3} \quad (17)$$

where Lewis number represents the ratio of the thermal diffusivity to the mass diffusivity.

The relationship between the relative humidity and the absolute humidity is estimated by Eq. (18).

$$\varphi = \frac{\omega P}{(0.622 + \omega)P_{sat,v}} \quad (18)$$

As given in Eq. (19), the saturation vapor pressure is calculated by Hyland-Wexler equation [31]:

$$P_{sat,v} = \exp\left[\sum_{i=-1}^{3} h_i T^i + h_4 \ln T\right] \quad (19)$$

where $h_{-1} = -0.580 \times 10^4$, $h_0 = 0.139 \times 10$, $h_1 = -0.486 \times 10^{-1}$, $h_2 = 0.418 \times 10^{-4}$, $h_3 = -0.145 \times 10^{-7}$, and $h_4 = 0.655$, which are valid for temperatures between 0°C and 200°C.

2.3 Air blower

As shown in Figure 3, the air supply system for PEMFC vehicles is composed of an air blower and a humidifier. The numerical model considers the temperature and pressure changes of the air when it passes through the air blower. The pressure ratio is determined by the blower map, with the air flow mass flow rate factor (MFF) as given in Eq. (20) [32, 33]:

$$MFF = \frac{\dot{m}\sqrt{T_{\text{air,ambient}}}}{P_{\text{air,ambient}}} \quad (20)$$

The temperature at the dry air inlet is calculated by Eq. (21):

$$T_{\text{dry,inlet}} = T_{\text{air,ambient}} + \frac{T_{\text{air,ambient}}}{\eta_{\text{blower}}}\left[\left(\frac{P_{\text{dry,inlet}}}{P_{\text{air,ambient}}}\right)^{\frac{\gamma-1}{\gamma}}\right] \quad (21)$$

where η_{blower} is the blower efficiency.

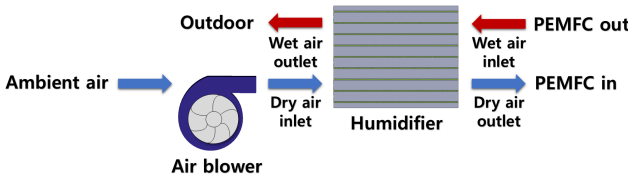

Figure 3: Schematic of the air supply system for PEMFC vehicles

2.4 Boundary conditions

For PEMFC vehicles, the operating conditions continuously change as the load changes. The required air flow rate for the PEMFC varies continuously corresponding to the current. Moreover, the air supplied to the PEMFC must be humidified. The dynamic response of the humidifier at various air flow rates needs to be analyzed to develop a control strategy to maintain the air temperature and relative humidity. The dry air entering into the plate-and-frame membrane humidifier was conditioned according to the air flow acceleration and sinusoidal air flow rate. The high acceleration of the air flow rate means a rapid increase in the velocity at the driving condition. The air flow rate was calculated based on the amount of the air required in the PEMFC. The baseline operating conditions in the humidifier are summarized in Table 2. The operating conditions were determined from experimental conditions used in the previous studies [24, 25]. The temperature at the dry air inlet varied in the range of 33.9–59.3°C under the simulation conditions. Transport properties including the thermal conductivity, heat capacity, and water diffusivity in the gas phase are shown in Table 3.

Table 2: Operating conditions

Parameters	Value
Ambient air pressure	101.35 kPa
Ambient air temperature	20°C
Ambient air relative humidity	0.01%
Wet air temperature	80°C
Wet air relative humidity	100%
Air flow rate	50 g s^{-1}–100 g s^{-1}
Air velocity in the channel	1.5 m s^{-1}–3 m s^{-1}

Table 3: Transport properties

Parameters	Value
Membrane [34, 35]	
Thermal conductivity	0.95 W $m^{-1}K^{-1}$
Heat capacity	4188 J $kg^{-1}K^{-1}$
Plate [36]	
Thermal conductivity	200 W $m^{-1}K^{-1}$
Heat capacity	719 J $kg^{-1}K^{-1}$
Air [15]	
Heat capacity	1006 J $kg^{-1}K^{-1}$
Water diffusivity in the gas phase	0.0000282 m^2 s^{-1}

3 Results and discussion

3.1 Effects of air flow acceleration

Figure 4 shows the variations in the air flow rate, temperature, absolute humidity, and relative humidity at the dry air outlet in response to the air flow acceleration. The difference between the peak and steady state values was defined as the overshoot or undershoot during the air flow change. The settling time was defined as the time required to reach 99% of the steady state value after the air flow rate change. As shown in Figure 4(a), the increasing slope of the air flow rate with respect to time increased with the increase in air flow acceleration from 0.05 to 1.0 m s^{-2}. As shown in Figure 4(b), for all air flow accelerations, the temperature at the dry air outlet decreased rapidly and reached the minimum value. After the undershoot, the temperature at the dry air outlet started to increase and then gradually approached the steady state value. However, as the air flow acceleration increased, the undershoot occurred earlier, owing to slow temperature change in the membrane and plate with low thermal diffusivity. Moreover, after the undershoot, the settling time decreased with the increase in air flow acceleration, because the inlet condition reached the steady state value quickly.

As shown in Figure 4(c), the undershoot of the absolute humidity at the dry air outlet occurred early, and the settling time decreased with the increase in air flow acceleration. In the plate-and-frame membrane humidifier, as shown in Figures 4(b) and 4(c), the mass transfer was faster than the heat transfer, because the settling time of the absolute humidity was shorter than that of the temper-

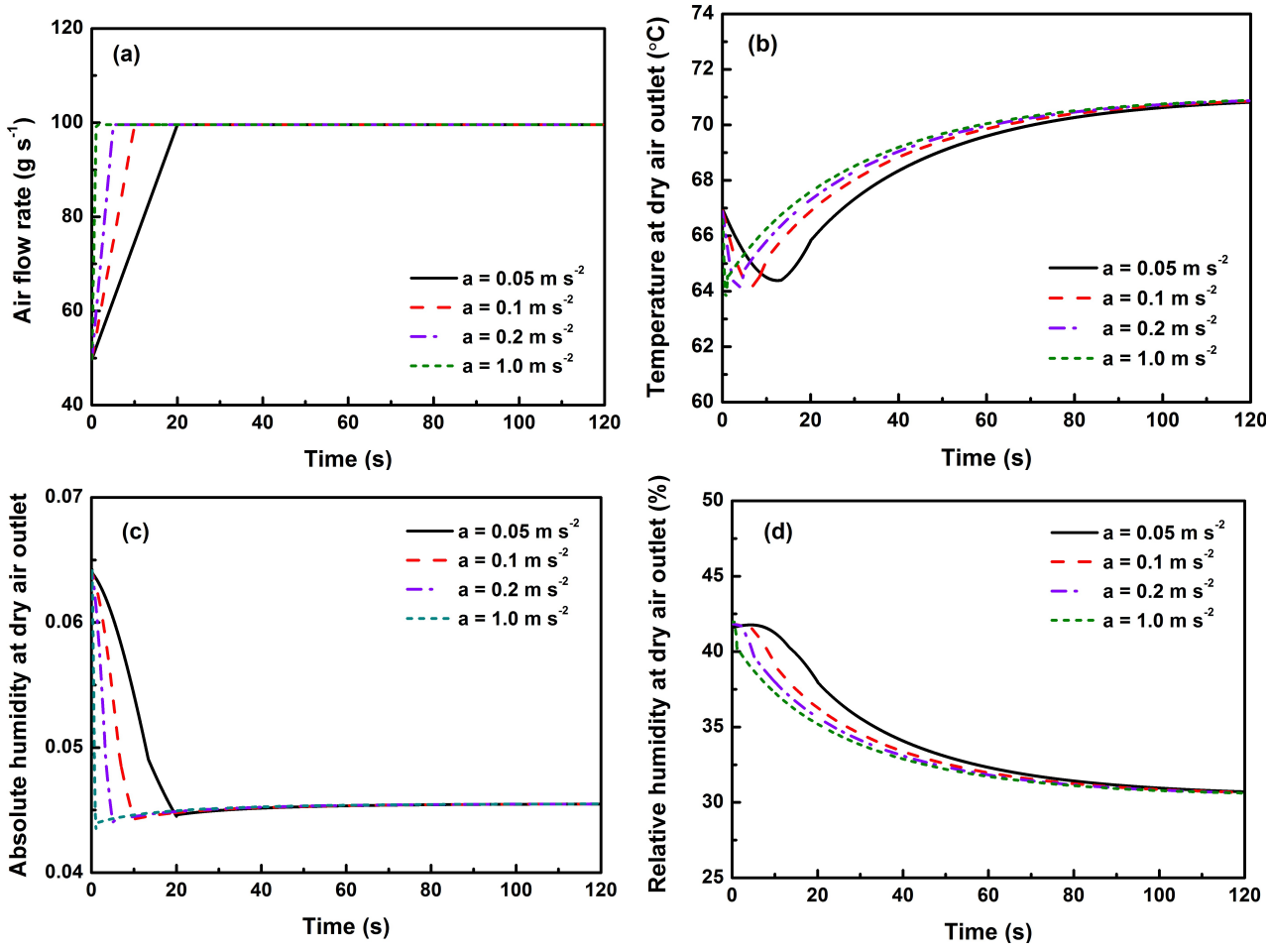

Figure 4: Variations of (a) air flow rate (b) temperature, (c) absolute humidity, and (d) relative humidity at the dry air outlet in response to change in air flow acceleration

ature. The plate where the heat transfer mainly occurred was about 20 times thicker than the membrane where the mass transfer mainly occurred.

The temperature and relative humidity at the dry air outlet are important parameters for the optimal control of PEMFC vehicles [37]. As shown in Figure 4(d), the settling time of the relative humidity at the dry air outlet decreased with the increase in the air flow acceleration because the relative humidity was affected by the absolute humidity and temperature. As the air flow acceleration increased, the relative humidity at the dry air outlet decreased rapidly, owing to the initial decrease in the absolute humidity. The relative humidity then approached the steady state value quickly, corresponding to the variation in temperature at the dry air outlet. Accordingly, higher air flow acceleration is more advantageous for PEMFC control owing to its fast responsiveness.

Figure 5 shows the effect of air flow acceleration on the average temperatures of the plate and membrane during the mass flow rate change. The average temperatures of the plate and membrane slowly increased with time, but the settling time of the plate with a larger heat capacity was longer than that of the membrane. At an air flow acceleration of 0.05 m s^{-2}, the average temperatures of the plate and membrane gradually and similarly increased, corresponding to the increase in the inlet temperature, owing to the gradual increase in the air flow rate. However, during 0 to 10 s with the rapid increase in the air flow rate, the average temperatures of the plate and membrane at an air flow acceleration of 1.0 m s^{-2} increased more slowly than those at an air flow acceleration of 0.05 m s^{-2}. The delay in heat transfer between the dry air and plate increased with the rapid increase in air flow acceleration. However, after 10 s, the average temperatures of the plate and membrane increased rapidly, owing to the dominant influence of the increased temperature at the dry air inlet. Therefore, the undershoot and settling time of the temperature at the dry

air outlet were affected by the temperature of the plate and membrane during the air flow rate change.

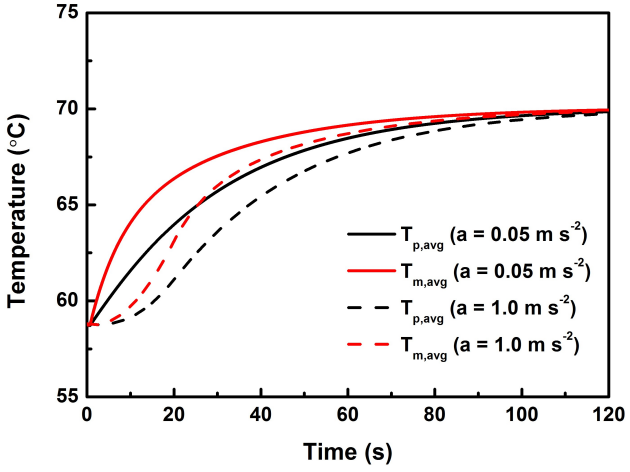

Figure 5: Effect of the air flow acceleration on plate and membrane average temperatures during mass flow rate change

Figure 6 shows variations in the dry air temperature and relative humidity of the dry air versus fractional distance in the air flow direction at an air flow acceleration of 1.0 m s^{-2}. When the dry air temperature was lower than the initial value (0 s), the undershoot was observed at the fractional distance in the air flow direction. Before 1 s, the undershoot of the dry air temperature was observed at the fractional distance between 0.6 and 1, because the effect of the air flow rate was larger than that of the inlet temperature. However, after 1 s, the dry air temperature increased above the initial temperature, owing to the increase in the effect of the increased inlet temperature. Before 0.5 s, the dry air relative humidity was close to the initial value at the fractional distance between 0.8 and 1, because the dry air temperature was lower than the initial value at the same time. However, after 0.5 s, the dry air relative humidity decreased with time for all fractional distances under the increased dry air temperature condition.

3.2 Effects of amplitude of sinusoidal air flow rate

As the PEMFC vehicle accelerates, the air flow rate increases because the PEMFC needs a large number of reactants instantaneously to raise the power. Accordingly, in actual driving conditions, the air flow rate varies corresponding to continuous periodic change between air flow acceleration and deceleration. In this study, when the air flow rate changed according to the sinusoidal function, the

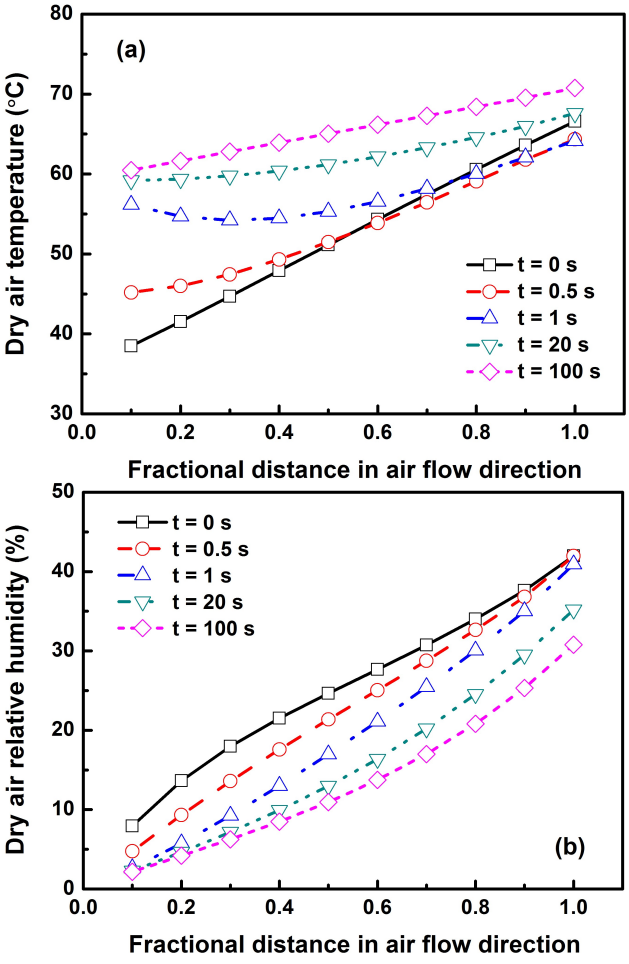

Figure 6: Profiles of (a) dry air temperature and (b) dry air relative humidity during mass flow change at 1.0 m s^{-2}

variations in the temperature and relative humidity were analyzed. The sinusoidal air flow rate is given by Eq. (22).

$$\dot{m}_{air,in} = A_{amp} \sin\left(\frac{2\pi t}{B_{peri}}\right) + 75 \tag{22}$$

where A_{amp} is the amplitude and B_{peri} is the period.

The global maximum and minimum temperatures and relative humidities are defined as the maximum and minimum values within one period, respectively. In addition, the local maximum and minimum temperatures and relative humidities are defined as the saddle points between these two values, respectively. The temperature and relative humidity differences between the global maximum and minimum values are given by Eqs. (23) and (24), respectively.

$$\Delta T_{global} = T_{\max,global} - T_{\min,global} \tag{23}$$

$$\Delta \varphi_{global} = \varphi_{\max,global} - \varphi_{\min,global} \tag{24}$$

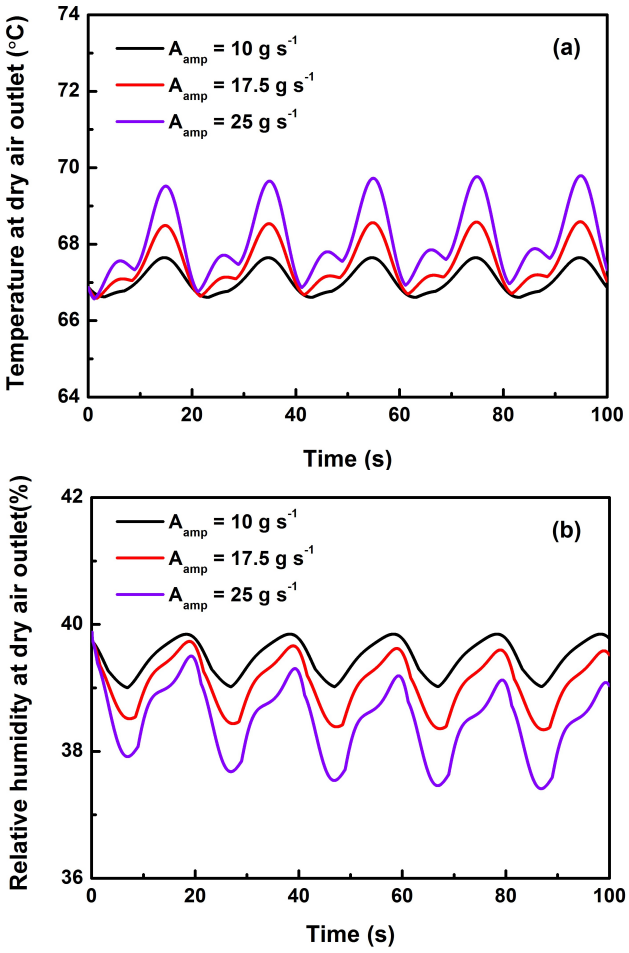

Figure 7: Variations of (a) temperature and (b) relative humidity at the dry air outlet with increase in the amplitude of the sinusoidal air flow rate from 10 to 25 g s^{-1}

Figure 7 shows the variations in the temperature and relative humidity at the dry air outlet in response to amplitude change with a period of 20 s. $\Delta T_{global,air}$ increased with the increase in the amplitude of the air flow rate because the variation in the temperature at the dry air inlet increased. In addition, while the variations in the temperature at the dry air outlet repeatedly increased and decreased at the amplitude of 10 g s^{-1}, the local maximum and minimum values occurred at amplitudes of 17.5 and 25 g s^{-1}, respectively. Overall, the nonlinearity in the temperature at the dry air outlet increased with the increase in the amplitude. Moreover, $\Delta\varphi_{global,air}$ increased with the increase in the amplitude of the relative humidity owing to the effect of $\Delta T_{global,air}$. Under the repeated air flow acceleration and deceleration conditions, the decrease in the amplitude is advantageous for controlling the PEMFC owing to the decrease in the temperature and relative humidity.

3.3 Effects of period of sinusoidal air flow rate

Figure 8 shows the variations in the temperature and relative humidity at the dry air outlet in response to the period change at an amplitude of 25 g s^{-1}. The local maximum and minimum temperatures at the dry air outlet were observed not only at a period of 10 s, but also at a period of 40 s. Even though the air flow acceleration decreased with the increase in the period, the nonlinearity in the temperature at the dry air outlet was not reduced by the increased period. Therefore, to reduce the nonlinearity with the sinusoidal air flow rate, it would be better to decrease the amplitude rather than to increase the period. In addition, $\Delta T_{global,air}$ for a 10 s period decreased more substantially than that for a 40 s period, because the delay in heat transfer increased with the increase in the air flow acceleration and deceleration. Moreover, $\Delta\varphi_{global,air}$ for a 10 s period decreased more substantially than that for a 40 s period, owing to increases in the delay in heat and mass transfer.

Figure 9 shows the variation in the average temperature of the plate in response to the period change. $\Delta T_{global,plate}$ decreased with the decrease in the period because the variation in the temperature of the plate was delayed at a larger heat capacity. The slow temperature change in the plate affected the maximum and minimum values of the dry air temperature and relative humidity in accordance with the period. As the period in the air flow rate decreased, the variations in the temperature and relative humidity at the dry air outlet also decreased owing to the influence between the plate and dry air. Therefore, to control the performance of the PEMFC under the repeated air flow acceleration and deceleration conditions, it would be preferable to decrease the period.

3.4 Model validation

The numerical model was validated by comparing the predictions with the experimental data in a plate-and-frame membrane humidifier reported by Yu [25]. The simulations were conducted using the developed numerical model at the same experimental conditions. As shown in Figure 10, the predicted mass flux and heat flux were compared with the experimental data at various dry air velocities. The predicted results showed a good agreement with the measured data within a deviation of ±9%.

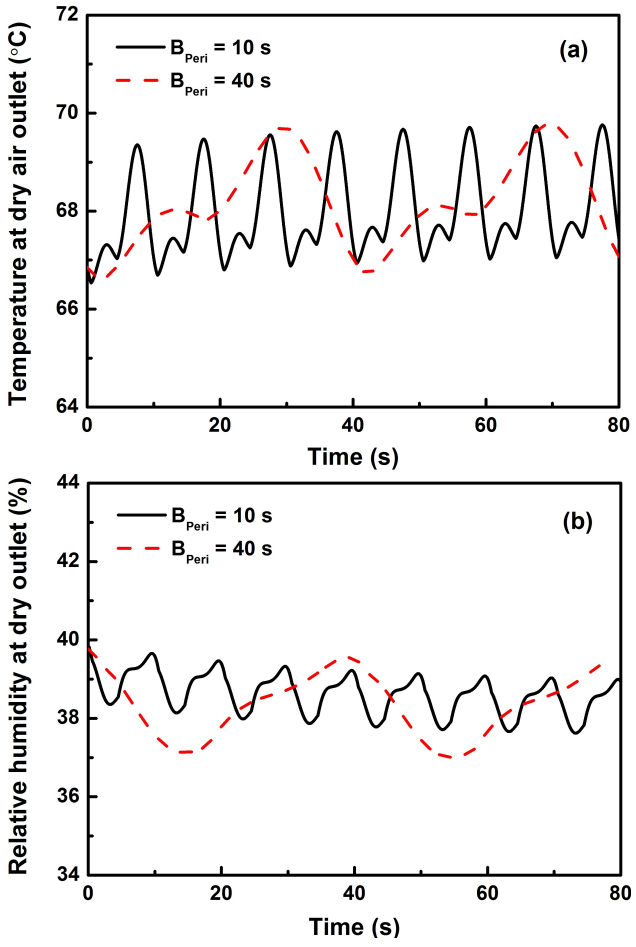

Figure 8: Variations of (a) temperature and (b) relative humidity at the dry air outlet with increase in the period of the sinusoidal air flow rate from 10 to 40 s

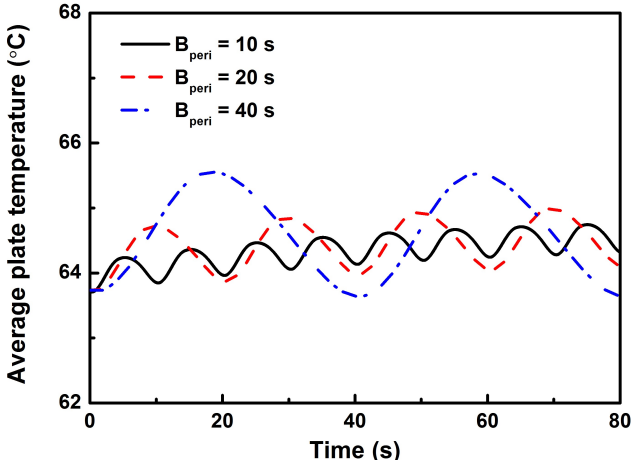

Figure 9: Effect of the period of the sinusoidal air flow rate on average plate temperature

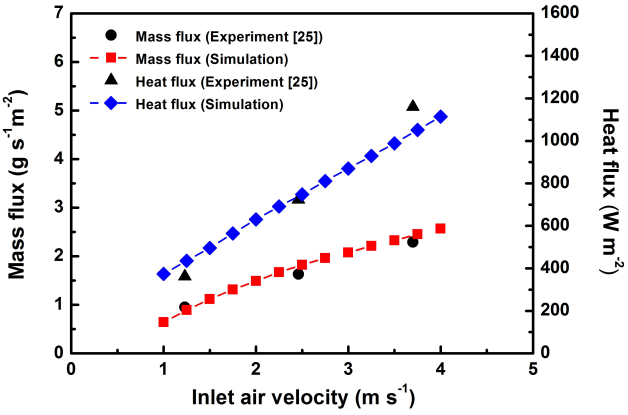

Figure 10: Comparison of the predictions with the measured data by Yu [25]

4 Conclusions

In this study, a pseudo-multi-dimensional dynamic model of a plate-and-frame membrane humidifier for PEMFC vehicles was developed in order to predict the heat and mass transfer performance under dynamic operating conditions. The numerical model was validated with experimental data. Based on the model developed, variations in the temperature and relative humidity at the dry air outlet in the plate-and-frame membrane humidifier were analyzed according to the air flow acceleration. The effects of heat transfer on the dynamic response of the plate-and-frame membrane humidifier are more dominant than those of mass transfer. The increased air flow acceleration was advantageous for the PEMFC control, due to its fast responsiveness. The dynamic response was also analyzed as a function of the amplitude and period of the sinusoidal air flow rate. Decreases in the amplitude and period of the air flow rate were advantageous for the PEMFC control owing to the decrease in the temperature and relative humidity difference between the maximum and minimum values. This study has some limitations on the consideration of the temperature and humidity variations at the humidifier inlet because the dynamic reaction in the PEMFC is not solved. Accordingly, further research is required on the dynamic response of PEMFC vehicle systems combining the plate-and-frame membrane humidifier and PEMFC under actual driving conditions.

Acknowledgement: This work was supported by the National Research Foundation of Korea (NRF) grant funded by the Korean Government (MSIP) (No. 2017R1A2B2003416).

References

[1] Wang Y., Chen K.S., Mishler J., Cho S.C., Adroher X.C., A review of polymer electrolyte membrane fuel cells: Technology, applications, and needs on fundamental research, Appl. Energy, 2011, 88, 981–1007.

[2] Wilberforce T., Alaswad A., Palumbo A., Dassisti M., Olabi A.G., Advances in stationary and portable fuel cell applications, Int. J. Hydrogen Energy, 2016, 41, 16509–16522.

[3] Kim B., Cha D., Kim Y., The effects of air stoichiometry and air excess ratio on the transient response of a PEMFC under load change conditions, Appl. Energy, 2015, 138, 143–149.

[4] Oh S.T., Saha B.B., Kariya K., Hamamoto Y., Mori H., Fuel cell waste heat powered adsorption cooling systems, Int. J. Air-Cond. Refrig., 2013, 21, 1350010.

[5] Cheng S., Xu L., Li J., Fang C., Hu J., Ouyang M., Development of a PEM fuel cell city bus with a hierarchical control system, Energies, 2016, 9, 417–435.

[6] Jeon S.W., Cha D., Kim H.S., Kim Y., Analysis of the system efficiency of an intermediate temperature proton exchange membrane fuel cell at elevated temperature and relative humidity conditions, Appl. Energy, 2016, 166, 165–173.

[7] Rojas A.C., Lopez G.L., Gomez-Aguilar J.F., Alvarado V.M., Torres C.L.S., Control of the air supply subsystem in a PEMFC with balance of plant simulation, Sustain., 2017, 9, 1–23.

[8] Wood D.L., Yi J.S., Nguyen T.V., Effect of direct liquid water injection and interdigitated flow field on the performance of proton exchange membrane fuel cells, Electrochim. Acta., 1998, 43, 3795–3809.

[9] Casalegno A., De Antonellis S., Colombo L., Rinaldi F., Design of an innovative enthalpy wheel based humidification system for polymer electrolyte fuel cell, Int. J. Hydrogen Energy, 2011, 36, 5000–5009.

[10] Huizing R., Fowler M., Mérida W., Dean J., Design methodology for membrane-based plate-and-frame fuel cell humidifiers, J. Power Sources, 2008, 180, 265–275.

[11] Kancsár J., Striednig M., Aldrian D., Trattner A., Klell M., Kügele C., et al., A novel approach for dynamic gas conditioning for PEMFC stack testing, Int. J. Hydrogen Energy, 2017, 42, 28898–28909.

[12] Chen X., Li W., Gong G., Wan Z., Tu Z., Parametric analysis and optimization of PEMFC system for maximum power and efficiency using MOEA/D, Appl. Therm. Eng., 2017, 121, 400–409.

[13] Chen C.Y., Yan W.M., Lai C.N., Su J.H., Heat and mass transfer of a planar membrane humidifier for proton exchange membrane fuel cell, Int. J. Heat Mass Transf., 2017, 109, 601–608.

[14] Chen X., Zhou H., Li W., Yu Z., Gong G., Yan Y., et al., Multi-criteria assessment and optimization study on 5 kW PEMFC based residential CCHP system, Energy Convers. Manage., 2018, 160, 384–395.

[15] Bhatia D., Sabharwal M., Duelk C., Analytical model of a membrane humidifier for polymer electrolyte membrane fuel cell systems, Int. J. Heat Mass Transf., 2013, 58, 702–717.

[16] Baharlou H.N., Afshari E., Three-dimensional CFD modeling of a planar membrane humidifier for PEM fuel cell systems, Int. J. Hydrogen Energy, 2014, 39, 14969–14979.

[17] Park S.K., Choe S.Y., Choi S.H., Dynamic modeling and analysis of a shell-and-tube type gas-to-gas membrane humidifier for PEM fuel cell applications, Int. J. Hydrogen Energy, 2008, 33, 2273–2282.

[18] Kang S., Min K., Yu S., Two dimensional dynamic modeling of a shell-and-tube water-to-gas membrane humidifier for proton exchange membrane fuel cell, Int. J. Hydrogen Energy, 2010, 35, 1727–1741.

[19] Zhang L.Z., Niu J.L., Effectiveness correlations for heat and moisture transfer processes in an enthalpy exchanger with membrane cores, J. Heat Transfer, 2002, 124, 922–929.

[20] Min J.C., Su M., Wang L.N., Experimental and theoretical investigations of membrane-based energy recovery ventilator performance, Int. J. Air-Cond. Refrig., 2012, 20, 1150004.

[21] Lee E.J., Lee J.P., Sim H.M., Kim N.H., Modeling and verification of heat and moisture transfer in an enthalpy exchanger made of paper membrane, Int. J. Air-Cond. Refrig., 2012, 20, 1250015.

[22] Kim N.H., Effect of the channel height of the enthalpy exchanger on energy saving by enthalpy recovery ventilator, Int. J. Air-Cond. Refrig., 2016, 24, 1650020.

[23] Kadylak D., Cave P., Mérida W., Effectiveness correlations for heat and mass transfer in membrane humidifiers, Int. J. Heat Mass Transf., 2009, 52, 1504–1509.

[24] Kadylak D., Mérida W., Experimental verification of a membrane humidifier model based on the effectiveness method, J. Power Sources, 2010, 195, 3166–3175.

[25] Yu S., Im S., Kim S., Hwang J., Lee Y., Kang S., et al., A parametric study of the performance of a planar membrane humidifier with a heat and mass exchanger model for design optimization, Int. J. Heat Mass Transf., 2011, 54, 1344–1351.

[26] Ahluwalia R.K., Wang X., Johnson W.B., Berg F., Kadylak D., Performance of a cross-flow humidifier with a high flux water vapor transport membrane, J. Power Sources, 2015, 291, 225–238.

[27] Han J., Yu S., Yi S., Advanced thermal management of automotive fuel cells using a model reference adaptive control algorithm. J. Hydrogen Energy, 2017, 42, 4328–4341.

[28] Incropera F., Dewitt D., Fundamental of heat and mass transfer, New York: John Wiley and Sons, 2002.

[29] Zhang L., Conjugate heat and mass transfer in heat mass exchanger ducts, Elsevier Science and Technology, 2013.

[30] Motupally S., Becker A.J., Weidner J.W., Diffusion of Water in Nafion 115 Membranes, J. Electrochem. Soc., 2000, 147, 3171–3177.

[31] Flatau P.J., Walko R.L., Cotton W.R., Polynomial fits to saturation vapor pressure, J. Appl. Meteorol., 1992, 31, 1507–1513.

[32] Bao C., Ouyang M., Yi B., Modeling and optimization of the air system in polymer exchange membrane fuel cell systems, J. Power Sources, 2006, 156, 232–243.

[33] James L., Dicks A., Fuel cell systems explained, John Wiley and Sons, 2003.

[34] Duy V.N., Lee J., Kim K., Ahn J., Park S., Kim T., et al., Dynamic simulations of under-rib convection-driven flow-field configurations and comparison with experiment in polymer electrolyte membrane fuel cells, J. Power Sources, 2015, 293, 447–457.

[35] Shah A.A., Ralph T.R., Walsh F.C., Modeling and simulation of the degradation of perfluorinated ion-exchange membranes in PEM fuel cells, J. Electrochem. Soc., 2009, 156, B465–B484.

[36] Shabalin I.L., Ultra-high temperature materials I: carbon (graphene/graphite) and refractory metals, Springer, 2014.

[37] Kanani H., Shams M., Hasheminasab M., Bozorgnezhad A., Model development and optimization of operating conditions to maximize PEMFC performance by response surface methodology, Energy Convers. Manag., 2015, 93, 9–22.